From localized discharge to distributed granular filtration on an inclined mesh

Javier Pillado [1,2] Valérie Vidal [3] Nicolás Taberlet [3] and Germán Varas [1,*]

[1] *Instituto de Fisica, Pontificia Universidad Católica de Valparaiso (PUCV), Avenida Universidad 330, Valparaiso, Chile*

[2] *Universidad Técnica Federico Santa María (USM), Avenida España 1680, Viña del Mar, Chile*

[3] *Laboratoire de Physique, École Normale Supérieure de Lyon–CNRS, 46 Allée d'Italie, 69364 Lyon Cedex 07, France*

(Received 27 May 2026; revised 31 August 2026; accepted 7 October 2026; published 26 October 2026)

Granular discharge through a single orifice is classically described by the Beverloo law, but this localized geometry becomes prone to clogging when the aperture size D is only a few grain diameters d. Here, we study dry avalanches of monodisperse glass beads over an inclined perforated mesh as a minimal system for distributed granular filtration. By measuring the mass passing through the mesh as a function of the downslope position, we show that the deposited mass profiles are independent of the initial released mass and are described by a spatial leakage law characterized by the filtration length ℓ. This length increases with the size ratio $\chi = d/D$, indicating that grain avalanches travel longer distances before being filtered as they approach the aperture width. In contrast to localized silolike discharge, which is suppressed beyond an aperture-size threshold, the inclined mesh remains operational over the explored range by providing a sequence of distributed passage opportunities. A comparison with localized discharge and a first-passage model identify the aperture-scale passage probability as the quantity controlling the macroscopic filtration length. These results connect Beverloo-type discharge, first-order sieving kinetics, and spatially distributed granular filtration.

DOI: 10.1103/wyc9-j9vn

I. INTRODUCTION

The gravity-driven discharge of granular materials through an orifice is a classical problem in granular physics, with direct relevance to silos, hoppers, and industrial handling processes [1,2]. For sufficiently large apertures, the mass flow rate is commonly described by the Beverloo law, $W = C\rho_b\sqrt{g}(D - kd)^{5/2}$, where W is the mass flow rate, ρ_b is the bulk density, D is the aperture size, d is the grain diameter, and C and k are empirical constants [1]. This expression naturally introduces the size ratio $\chi = d/D$, which compares the grain diameter with the aperture size. Although the Beverloo scaling has been rationalized in terms of the density and velocity fields near the outlet [3,4], it also highlights a geometric limitation: as χ increases, the discharge becomes increasingly susceptible to clogging through stable arches and intermittent jamming events [5–8].

Many separation systems avoid a single bottleneck and instead use perforated surfaces, where grains progressively leave a flowing layer through many apertures distributed along the flow direction [9–12]. In this case, the relevant quantity is not only the instantaneous discharge rate but also the spatial rate at which material is removed from the flow. Classical and probabilistic models of sieving describe this removal as a first-order process in time or along the screen, or equivalently as the result of repeated passage attempts [9–11]. In these descriptions, an exponential decrease of the retained or flowing mass is expected when the probability of passage per unit length is approximately constant. However, stratification, bed depth, crowding, and near-aperture-size particles may produce deviations from this effective behavior [10–12]. Moreover, even in multiple-orifice silos, neighboring openings can interact through their flow fields, leading to nontrivial discharge rates and kinematics with respect to independent single-orifice predictions [13,14]. Thus, a perforated surface cannot generally be treated as N independent Beverloo outlets.

Here, an avalanche denotes one complete release of a finite mass from the funnel and its subsequent downslope motion over the mesh until all grains are collected. We study distributed granular filtration during such dry avalanches of monodisperse glass beads. By measuring the mass passing through the mesh as a function of the downslope position, we first characterize the spatial deposition profile and test its dependence on the initial released mass. We then show that the filtration process is captured, under the explored conditions, by a spatial leakage law characterized by a filtration length, and we determine how this length varies with χ. Finally, we contrast this distributed-filtration regime with a localized reference discharge near the aperture-size limit.

II. EXPERIMENTAL SETUP

Dry-avalanche experiments were performed by releasing an initial mass M_0 of monodisperse glass beads from a funnel with a fixed rectangular outlet of 8×15 cm^2 onto a 70-cm-long and 10-cm-wide three-dimensionally (3D) printed PLA mesh inclined at $\theta = 18^\circ$ with respect to the horizontal (Fig. 1). All experiments were performed at this fixed inclination. The angle was selected empirically to ensure

*Contact author: german.varas@pucv.cl

 ©2026 American Physical Society

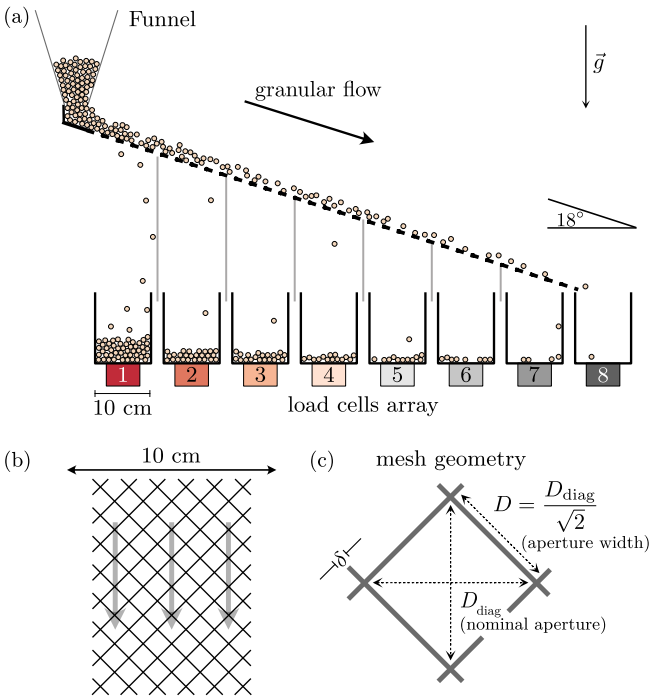


FIG. 1. Experimental setup and mesh geometry. (a) Grains released from a funnel with its outlet positioned 25 mm above the mesh flow downslope over an inclined perforated mesh at $\theta = 18^\circ$ and are collected in eight load-cell bins: seven bins below the filtering region and one downstream bin for the residual mass. Gray vertical lines indicate paper guides between bins. (b) Top view of a representative mesh section. Gray arrows indicate the downslope flow direction. (c) Square aperture geometry, with nominal diagonal aperture D_{diag}, aperture width $D = D_{\text{diag}}/\sqrt{2}$, and mesh-bar thickness $\delta = 0.7$ mm. The size ratio is $\chi = d/D$.

sustained downslope transport while allowing sufficient interaction between the grains and the apertures: in preliminary tests, the grains flowed reproducibly without external forcing, measurable deposition was obtained along the filtering region, and the residual collector downstream of the mesh did not dominate the collected mass. No systematic inclination sweep was performed, and the flowing-layer thickness was not measured directly. The 3D-printed mesh bars have a thickness $\delta = 0.7$ mm. The value of M_0 was varied between 250 and 1750 g in a set of control experiments.

As the grains flow downslope, part of the material progressively passes through the mesh and is collected in a series of 10-cm-long bins mounted on load cells (Phidgets, single-point load cell C4, 3 kg), allowing us to measure the spatial distribution of the filtered mass along the slope. Seven bins are located below the mesh, covering the filtering region, while an eighth bin is positioned at the downstream end to recover the residual mass. Thin paper guides inserted between neighboring bins direct the falling grains into the corresponding collector and prevent lateral spreading or transfer between adjacent bins. The load-cell signals are recorded at 100 Hz throughout the avalanche, and the final mass collected in each bin is used to infer the deposited mass profile. Each experimental condition is repeated three times to check reproducibility.

We used glass beads with diameters $d = 1,\ 1.5,\ 3,\ 4$, and 5 mm on meshes with nominal diagonal apertures $D_{\text{diag}} = 12$ and 9 mm. For the square openings used here, the corresponding aperture width is $D = D_{\text{diag}}/\sqrt{2}$, giving $D = 8.48$ and 6.36 mm, respectively. Additional tests in which the mesh was rotated so that the square openings were aligned with the downslope direction did not show significant changes in the deposited mass profiles, indicating that the aperture width, rather than the diagonal orientation, is the relevant geometric scale. Smaller nominal apertures were not included in the systematic study because the 3D printing process produced rounded or partially obstructed openings. In preliminary tests, these defects reduced the effective local aperture and produced persistent clogging; these meshes were therefore excluded. The experiments are characterized by the dimensionless size ratio $\chi = d/D$, which compares the grain diameter to the aperture width. The explored range was $0.12 \lesssim \chi \lesssim 0.79$, spanning from grains much smaller than the aperture width to near-aperture-size particles.

III. RESULTS

The load-cell signals provide a direct measurement of how the avalanche is progressively filtered along the inclined mesh. For each bin i, we denote by $m_i(t)$ the mass collected up to time t, and by $m_i = m_i(\infty)$ we denote its final plateau value. The downstream bin collects the residual material that does not pass through the mesh, and no grains were observed to remain trapped in the apertures after the avalanche. The total collected mass therefore accounts for the released mass M_0 to within 1%. We define the final deposited mass fraction as

$$\mu_i = \frac{m_i}{M_0}, \tag{1}$$

and we use the corresponding time-dependent fraction $m_i(t)/M_0$ to describe the filling dynamics. For bins 1–7, μ_i is the normalized mass collected over a finite width of $\Delta x = 10$ cm, and bin 8 instead measures the residual fraction that leaves the downstream edge of the mesh.

Figure 2(a) shows a representative experiment in which the mass fraction collected by each bin increases during the passage of the flow avalanche and then reaches a plateau. The upstream bins receive most of the material, while the downstream bins collect progressively smaller amounts, indicating that the flowing layer is depleted as it travels along the mesh.

The plateau values of the load-cell signals give the final deposited mass profile along the slope. As shown in Fig. 2(b), this profile decreases rapidly with the downslope position: most grains pass through the first part of the mesh, while only a small fraction reaches the downstream collectors. A simple exponential fit captures this spatial decay, suggesting that the avalanche loses a nearly constant fraction of its remaining mass per unit length. This observation motivates the spatial leakage description developed below.

To test whether the spatial deposition pattern depends on the total amount of material supplied, we varied the initial released mass from $M_0 = 250$ to 1750 g for selected particle-mesh combinations. As shown in Fig. 3(a), the normalized deposition profiles μ_i collapse, to a good approximation,

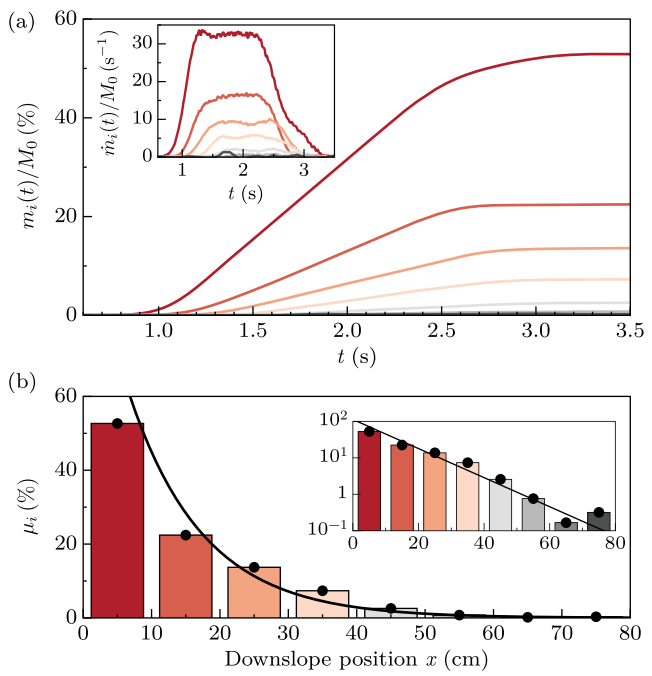


FIG. 2. Representative distributed-filtration experiment ($\chi = 0.35$, $M_0 = 1$ kg). (a) Temporal evolution of $m_i(t)/M_0$ in each load-cell bin. The inset shows the corresponding normalized collection rates $\dot{m}_i(t)/M_0$. (b) Final mass fraction per collector μ_i versus downslope position x. The black curve is an exponential fit considering bins 1–7. Bin 8 reports the residual fraction and is not included in the fit, and the inset shows the same profile in semilog scale.

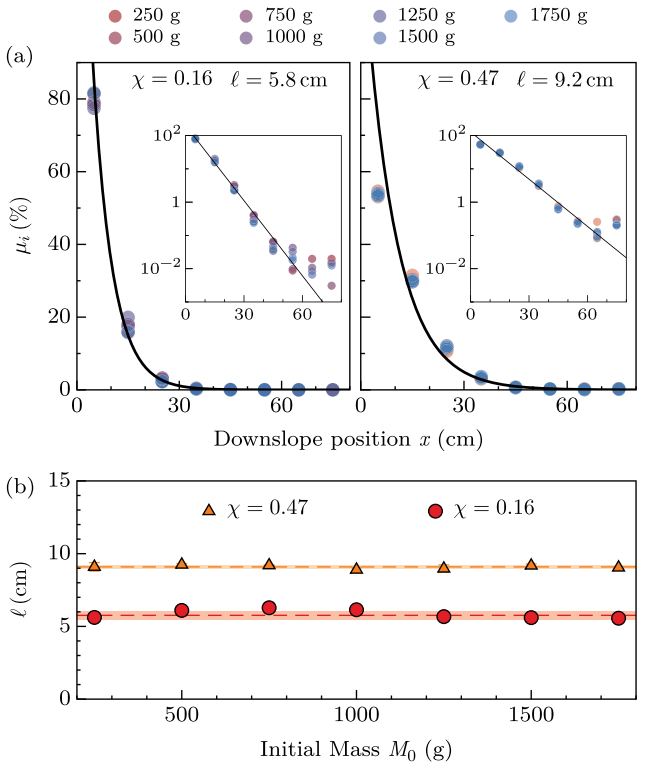


FIG. 3. Effect of released mass on spatial filtration. (a) Final deposited fraction μ_i for different M_0 values and two representative values of $\chi = d/D$. Black curves are fits $\mu_i \sim \exp(-x/\ell)$. Insets show semilog representations. (b) Mean filtration length ℓ obtained by fitting each realization independently. The shaded bands denote the standard deviation and dashed lines denote the averages over M_0. Filtration length ℓ from individual profile fits versus M_0. Dashed lines indicate mean values. Error bars smaller than the symbols are not visible.

for different values of M_0. The largest deviations occur for the smallest released masses, where fewer grains sample the mesh. Nevertheless, the characteristic spatial decay of the profiles remains approximately unchanged over the explored range, as shown in Fig. 3(b). The variability between realizations is small. In Fig. 3(a), the corresponding standard deviations are mostly smaller than the symbols and are therefore not shown. In Fig. 3(b), the vertical error bars report the standard deviation of the fitted values of ℓ and are also mostly smaller than the symbols. This indicates that the spatial distribution of deposited mass is not primarily controlled by the total released mass, but by the local interaction between flowing grains and the mesh geometry. The weak dependence on M_0 allows us to use $M_0 = 1$ kg in the remainder of the study.

The collapse of the normalized profiles motivates a minimal spatial leakage model, in which the rate of mass loss per unit distance is proportional to the mass still flowing on the mesh. This is the spatial analog of first-order sieving kinetics, where the removal rate is proportional to the amount of material remaining to be screened. It can also be interpreted probabilistically: if grains experience repeated passage attempts along the mesh, each with an effective probability of success, the fraction remaining on the surface decreases exponentially with the downslope distance [9,10].

Let $M(x)$ be the mass still flowing on the mesh after traveling a downslope distance x. If the probability of passing through the mesh per unit length is approximately constant, then the loss of flowing mass is proportional to the mass still available,

$$\frac{dM}{dx} = -\frac{1}{\ell}M(x), \tag{2}$$

which gives

$$M(x) = M_0 e^{-x/\ell}. \tag{3}$$

The deposited mass per unit length is therefore proportional to $-dM/dx$ and also decays exponentially along the slope. The measured quantity, however, is the mass integrated over a finite bin. For bin i, extending from x_i^- to $x_i^+ = x_i^- + \Delta x$, the normalized mass reads

$$\mu_i = \frac{1}{M_0}\int_{x_i^-}^{x_i^+}\left(-\frac{dM}{dx}\right)dx = e^{-x_i^-/\ell}\left(1 - e^{-\Delta x/\ell}\right). \tag{4}$$

Because bins 1–7 have the same width, the factor in parentheses only changes the prefactor. Fits to $A\exp(-x/\ell)$ with the free amplitude A therefore give the same decay length. Bin 8 is excluded because it measures the residual mass beyond the mesh rather than deposition over another interval.

The parameter ℓ is the characteristic filtration length: small ℓ corresponds to rapid filtration near the entrance of the mesh, whereas large ℓ indicates that grains travel farther before

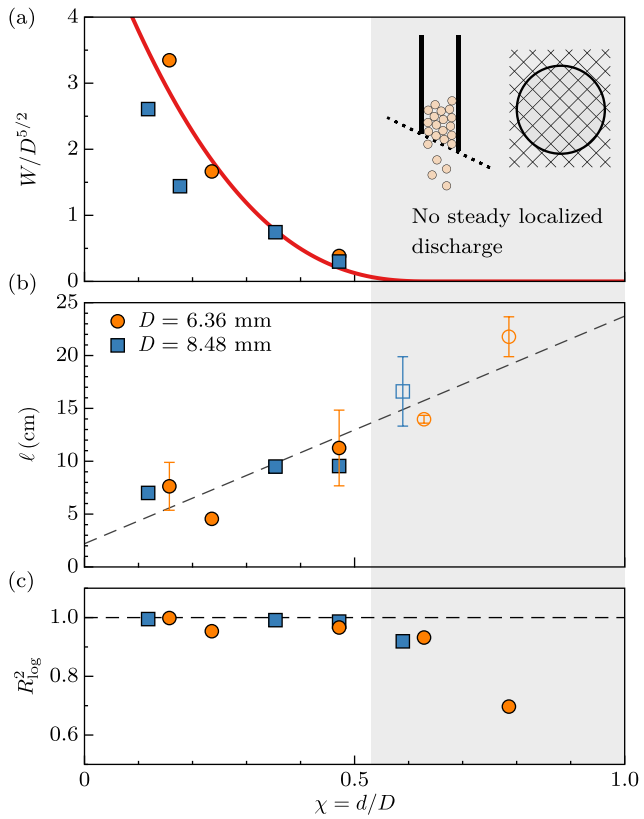


FIG. 4. Localized silolike discharge and distributed filtration as functions of $\chi = d/D$. (a) Results from a reference localized-discharge experiment. Grains are discharged from a vertical cylinder placed above the inclined mesh, restricting the outflow to a finite patch of apertures, as sketched in the inset. The red curve is a Beverloo-type scaling, $W/D^{5/2} = A(1 - k\chi)^{5/2}$, fitted in the stable-discharge range. The shaded region marks conditions for which no steady discharge was observed in five tests. (b) Filtration length ℓ obtained from the inclined-mesh avalanche experiments. Solid symbols denote conditions for which a single exponential well describes the deposited-mass profiles. Open symbols indicate the largest size ratios, $\chi > 0.5$, where ℓ is retained as an effective fitted transport length. (c) Logarithmic coefficient of determination $R^2_{\ln}$ for the same exponential fits used in panel (b). Values close to unity indicate a good single-exponential description. The vertical shaded region marks the range in which no steady localized discharge was observed in the reference configuration.

being collected, as shown in Fig. 3(a). The weak variation of ℓ with the released mass, shown in Fig. 3(b), indicates that this length is mainly controlled by the particle-mesh geometry rather than by the total amount of material supplied. Thus, ℓ provides a simple quantitative descriptor of how rapidly the flowing layer is depleted along the slope.

This filtration length also allows the inclined-mesh experiments to be compared with a localized discharge geometry [Fig. 4(a)]. In the reference experiment, grains were discharged from a vertical cylinder with a diameter of 50 mm placed above the inclined mesh, restricting the outflow to a finite patch of apertures rather than distributing it over the full inclined surface. Each experimental condition in this reference configuration was repeated five times. The relevant observable in this localized configuration is the steady instantaneous mass flow rate W, which becomes increasingly sensitive to aperture size as the grains approach the opening width. Previous studies of classical silo discharge report clogging when the aperture is only a few grain diameters wide, corresponding to thresholds of order $\chi = d/D \simeq 0.2$–0.33, depending on dimensionality, outlet geometry, and particle properties [5,7,8,15]. The precise value also depends on how the aperture length is defined: a circular outlet is naturally described by its diameter, whereas for the square openings used here we take D as the aperture width. In our localized reference geometry, steady discharge is suppressed at larger χ, consistent with the geometry-dependent nature of clogging. Writing the Beverloo law [1] in terms of the size ratio $\chi = d/D$ gives

$$\frac{W}{D^{5/2}} = A(1 - k\chi)^{5/2}, \tag{5}$$

where $A = C\rho_b\sqrt{g}$ is treated here as an effective prefactor, with $\rho_b = 1538$ kg/m^3 being the measured bulk density of the glass beads sample. Figure 4(a) shows the normalized localized-discharge rate $W/D^{5/2}$ as a function of χ. The red curve is a Beverloo-type scaling fitted in the stable-discharge range, while the shaded region marks the range in which steady localized discharge was not observed.

The inclined mesh operates differently from the localized discharge geometry. Since grains remain mobile along the slope, blocking or inefficient passage through a single aperture does not stop the entire process; instead, grains continue downslope and encounter additional openings. The same shaded region is repeated in Fig. 4(b) to show that distributed filtration persists in a range where localized discharge is suppressed. Note that this comparison is geometric and operational, the filtration law is not derived from Beverloo. Thus, approaching the aperture-size limit does not abruptly arrest filtration, but increases the distance grains must travel before passing through the mesh. Figure 4(c) shows $R^2_{\ln}$ for the same exponential fits used to obtain ℓ in Fig. 4(b). The single-exponential description remains accurate at small and intermediate χ, but progressively deteriorates for the largest size ratios, $\chi > 0.5$. The corresponding open symbols in Fig. 4(b) are therefore retained as effective fitted transport lengths rather than strict exponential decay lengths. Representative profiles and details of the calculation are provided in Appendix B.

This behavior can be interpreted as a spatial first-passage process, where the normalized remaining mass $S(x) = M(x)/M_0$ is the fraction of material that has not yet passed through the mesh. Suppose that grains encounter passage opportunities separated by an effective distance ξ and that the probability of successful passage at each opportunity is $p(\chi)$. After a distance $x = n\xi$,

$$S(x) = \frac{M(x)}{M_0} = [1 - p(\chi)]^n = \exp\left[-\frac{x}{\ell(\chi)}\right], \tag{6}$$

which gives

$$\ell(\chi) = \frac{\xi}{-\ln[1 - p(\chi)]}. \tag{7}$$

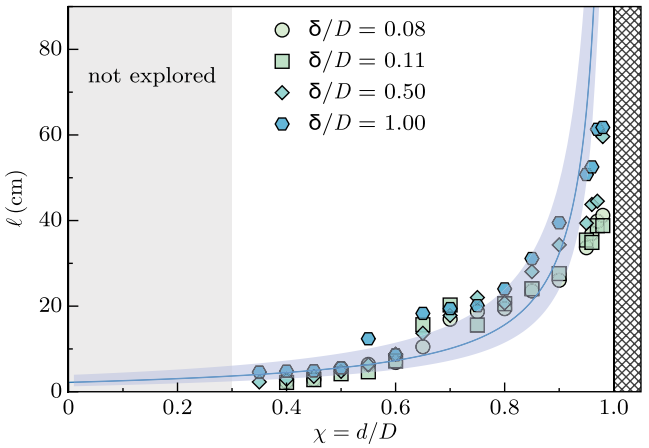


FIG. 5. Filtration length from 2D DEM simulations. The data show the filtration length ℓ as a function of $\chi = d/D$ for different mesh-bar thicknesses δ/D. The solid curve shows the first-passage model $\ell(\chi) = \xi/\{-\ln[1 - p_0(1-\chi)]\}$, using $\xi = 2$ cm and $p_0 = 0.6$. The shaded band indicates the range obtained for $0.4 \leqslant p_0 \leqslant 0.8$. The left shaded region indicates rapid-filtration cases where ℓ was not extracted because too few spatial bins contained significant mass. The hatched region marks the geometrically forbidden limit $\chi \geqslant 1$.

Here ξ is an effective distance between independent passage attempts, while $p(\chi)$ includes not only geometric accessibility but also the position, velocity, and local contact configuration of the grains.

As a minimal geometric assumption, we take the passage probability to be proportional to the relative free aperture,

$$p(\chi) = p_0(1-\chi), \tag{8}$$

where $p_0 < 1$ is the basal passage probability for a pointlike particle. This gives

$$\ell(\chi) = \frac{\xi}{-\ln\,[1 - p_0(1-\chi)]}. \tag{9}$$

This expression predicts a finite value $\ell(0) = \xi/[-\ln(1 - p_0)]$, because even very small grains must encounter a favorable passage opportunity, and a divergence $\ell \simeq \xi/[p_0(1-\chi)]$ as $\chi \to 1$, when the passage probability vanishes.

To test this interpretation beyond the experimental range, we performed two-dimensional discrete-element-method (2D DEM) simulations using initial conditions analogous to the experiments (see Appendix A). The simulations provide a controlled way to extend the size ratio up to $\chi \simeq 0.98$ and to vary the normalized mesh-bar thickness δ/D independently (Fig. 5). Although they are not meant to reproduce the experiments quantitatively, they show the same trend: ℓ grows weakly at small and intermediate χ and rises rapidly near the aperture-size limit. Over the simulated range, this trend is only weakly affected by δ/D, suggesting that the dominant control parameter is the relative grain-to-aperture size $\chi = d/D$.

The left shaded region marks the low-χ range where ℓ was not extracted: filtration is so rapid that most grains pass through the mesh within the first few bins, leaving too few points for a meaningful exponential fit. This is therefore a limitation of the spatial resolution of the analysis, not a physical absence of filtration. The curve in Fig. 5 uses $\xi = 2$ cm and $p_0 = 0.6$, while the shaded band shows representative variations of p_0. These curves should be read as a mechanistic scaling argument rather than as precise fits. Despite the difficulty of determining ξ and p_0 independently, the agreement over the simulated range is reasonable, supporting the first-passage interpretation as an effective description of the filtration process. In this framework, ξ and p_0 encode the effects of mesh architecture and flow dynamics, including aperture spacing, mesh-bar thickness, inclination, flow velocity, flowing-layer thickness, friction, and crowding, among other factors.

IV. CONCLUSION

We have studied dry avalanches of monodisperse grains over an inclined perforated mesh as a minimal model for distributed granular filtration. Within the tested range, the normalized deposited-mass profiles are largely insensitive to the initial released mass. For small and intermediate values of χ, the profiles are well described by a single-exponential spatial leakage law. At the largest size ratios, systematic deviations emerge, and the fitted filtration length ℓ should be interpreted as an effective measure of the spatial extent of particle transport rather than as a strict exponential decay length.

Compared with localized Beverloo-type discharge, the inclined mesh replaces a clogging-prone confined outlet region by a spatially extended sequence of passage opportunities. As a result, filtration remains operational over a range of size ratios where steady localized discharge is not observed, although the filtration length increases as grains approach the aperture width. The first-passage interpretation shows that this increase can be understood as the macroscopic signature of a decreasing aperture-scale passage probability, characterized by an effective sampling length ξ and a basal passage probability p_0. These effective parameters depend on mesh architecture and flow conditions and are not expected to be universal. These results connect classical orifice discharge, first-order sieving kinetics, and distributed granular filtration, providing a simple framework for comparing and designing mesh-based separation systems, from industrial sieving to granular cleaning applications.

Beyond the present model system, this distributed geometry suggests a passive route for controlling granular screening and dosing. Within the regime where the single-exponential description applies, the leakage model predicts that a mesh of length L filters a fraction, $1 - e^{-L/\ell}$, of the initial mass. The partition between material collected through the mesh and residual material leaving its downstream end could therefore, in principle, be tuned through χ, L, and θ. Such control could provide a passive means of controlling the removed or residual fraction in gravity-driven screening and dosing systems for a wide range of applications, ranging from beach cleaning machines to medication dosing. Establishing this design potential will require systematic measurements of inclination, inlet flow rate, flowing-layer thickness, aperture geometry, and particle-size distribution.

ACKNOWLEDGMENTS

The authors acknowledge financial support from the Chilean Agency ANID through BECAS/DOCTORADO NACIONAL Grant No. 21110001 and FONDEF Grant No. 23I10249.

DATA AVAILABILITY

There are no publicly available research data or software supporting this manuscript. Requests for further information or data should be sent to the authors.

APPENDIX A: NUMERICAL SIMULATION DETAILS

We perform two-dimensional discrete element method (DEM) simulations of granular discharge over an inclined perforated mesh. The simulations are not intended as a full three-dimensional reconstruction of the experiment, but as a controlled particle-scale model to test how the filtration length ℓ varies with the grain-to-aperture ratio $\chi = d/D$ and with the normalized mesh-bar thickness δ/D. The numerical model follows the standard DEM description of particle motion and frictional contacts introduced by Cundall and Strack [16] and, for granular-flow applications, reviewed by Guo and Curtis [17].

1. Geometry and initial condition

The grains are modeled as identical soft disks of diameter $d = \chi D$, where $D = 8.48$ mm is the aperture width used in the main text. The mesh is represented as a sequence of open intervals of width D, separated by solid bars of thickness δ. Thus, the aperture pitch is

$$p = D + \delta = D(1 + \delta/D). \tag{A1}$$

The simulations use a mesh length of $L = 1.5$ m, an inclination angle of $\theta = 18^\circ$, and an upstream solid section of length 10 cm, where the apertures are closed. The number of plugged apertures is computed as round $(10\ \text{cm}/p)$, so the actual plugged length changes slightly with δ/D. Downstream of this region, each collecting bin corresponds to one open aperture, keeping the bin definition consistent when δ/D is varied.

The material is initially placed in a feeder formed by a vertical upstream wall and a diagonal wall, with an outlet width of 4.0 cm near the beginning of the mesh. Particles are generated in a reproducible hexagonal-like packing using a fixed random seed, with zero mean downslope velocity and a small random velocity perturbation of amplitude 0.015 m s^{-1}. Although the disks are monodisperse, the initial order is rapidly lost once the grains leave the feeder and interact with the inclined mesh, so no size polydispersity is introduced. This produces a gently released avalanche rather than a preaccelerated stream.

2. Equations of motion and contacts

For each active disk i, we integrate the translational and rotational dynamics

$$m_i \dot{\boldsymbol{v}}_i = \sum_j \boldsymbol{F}^c_{ij} + m_i \boldsymbol{g} - \gamma_g \boldsymbol{v}_i, \tag{A2}$$

$$I_i \dot{\omega}_i = \sum_j \tau^c_{ij}. \tag{A3}$$

Here m_i and I_i are the mass and moment of inertia, $\boldsymbol{v}_i$ and ω_i are the translational and angular velocities, $\boldsymbol{F}^c_{ij}$ and τ^c_{ij} are the contact force and torque on i, and $m_i \boldsymbol{g}$ is the gravity. The term $-\gamma_g \boldsymbol{v}_i$ is a weak global linear damping force, proportional to the disk velocity, and $\boldsymbol{g} = (0, -9.81)$ m s^{-2}. For the two-dimensional disks,

$$m_i = \rho_{2\mathrm{D}} \pi r_i^2, \qquad I_i = \tfrac{1}{2} m_i r_i^2, \tag{A4}$$

where $r_i = d/2$. Particle rotations are included, but no rolling resistance or angular drag is used. Time integration uses a semi-implicit Euler-Cromer scheme, with a time step chosen from the estimated contact time [18].

Contacts are modeled with a linear spring-dashpot normal force and a regularized tangential friction capped by Coulomb friction,

$$\boldsymbol{F}_n = F_n \boldsymbol{n}, \qquad F_n = \max(0, k_n \eta - \gamma_n v_n), \tag{A5}$$

$$F_t = \mathrm{clip}(-\gamma_t v_t,\ -\mu F_n,\ \mu F_n). \tag{A6}$$

Here η is the overlap, v_n and v_t are the normal and tangential relative velocities, and $\boldsymbol{n}$ is the contact normal. The same contact law is used for particle-particle and particle-wall contacts, with different friction coefficients. The time step satisfies $\Delta t < 0.15\ t_c$, where t_c is the estimated contact time. The parameters used in the simulations are summarized in Table I.

3. Dependence on bin width

To test the robustness of ℓ, we repeat the analysis after grouping neighboring aperture bins into coarser spatial bins of

TABLE I. DEM and geometry parameters used in the simulations.

Quantity	Symbol(s)	Value(s)
Disks	N	1500
Mesh geometry	$L,\ \theta,\ D$	1.5 m, 18°, 8.48 mm
Mesh-bar thickness ratio	δ/D	0.08, 0.11, 0.5, 1.0
Particle density and gravity	$\rho_{2\mathrm{D}},\ g$	1538 kg m^{-2}, 9.81 m s^{-2}
Normal contact	$k_n,\ \gamma_n$	1.65×10^5 N m^{-1}, 16 kg s^{-1}
Tangential contact	$\gamma_t,\ \mu_{pp},\ \mu_{pw}$	5.5 kg s^{-1}, 0.46, 0.42
Global linear damping	γ_g	0.055 kg s^{-1}
Integration window	$\Delta t,\ t_{\max}$	3.0×10^{-5} s, 7 s

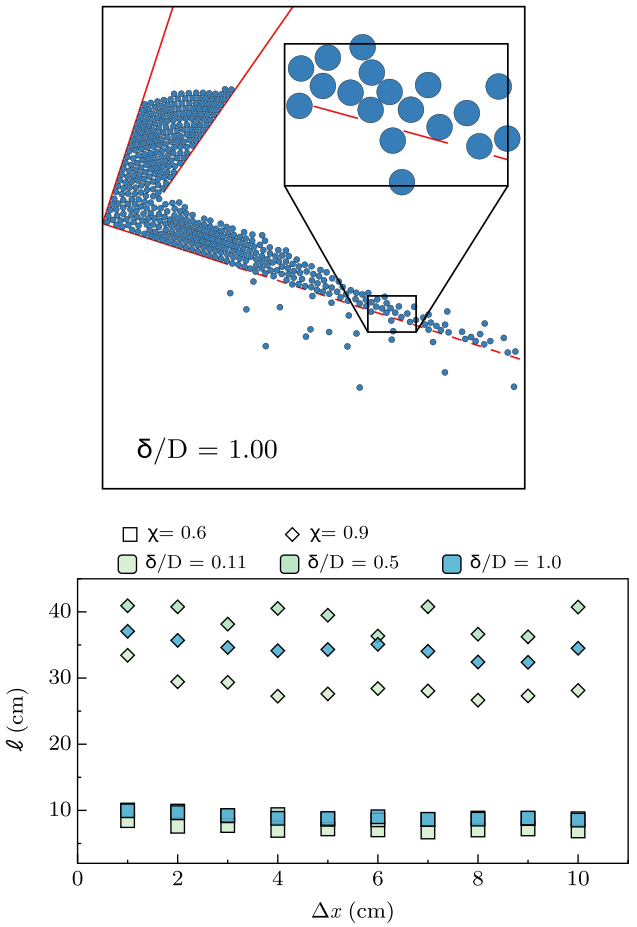


FIG. 6. (a) DEM snapshot for $\chi = 0.60$ and $\delta/D = 1$, showing a portion of the simulated domain near the mesh. The inset magnifies the particle-aperture region. (b) Sensitivity of the extracted filtration length ℓ to the bin width Δx for representative values of χ and δ/D.

width Δx (see Fig. 6). For the simulations reported in the main text, each bin corresponds to one open aperture. The weak dependence of ℓ on Δx indicates that the extracted length is robust over the range used in the main text.

APPENDIX B: LIMITS OF THE EXPONENTIAL DESCRIPTION

To assess the range of validity of the single-exponential description, Fig. 7 shows the experimental deposited-mass profiles for five representative values of $\chi = d/D$ at $M_0 = 1$ kg. The solid lines are fits of the form $f(x) = A\exp(-x/\ell)$. The residual collector at $x = 75$ cm is shown for completeness but is excluded from the fits and from the following analysis. For small and intermediate values of χ, the profiles are well described by a single exponential. As χ increases, systematic deviations develop, becoming most pronounced for $\chi = 0.63$ and 0.79.

We quantify the quality of the exponential description in logarithmic space, where an exponential profile becomes linear. The coefficient of determination is defined as

$$R^2_{\log} = 1 - \frac{\sum_i [\ln f_i - \ln f_i^{\mathrm{fit}}]^2}{\sum_i [\ln f_i - \langle \ln f \rangle]^2}. \tag{B1}$$

Thus, $R^2_{\log} = 1$ corresponds to a perfect exponential profile, while decreasing values indicate increasing deviations from exponential behavior. The coefficient is evaluated using all filtering bins for which $\mu_i > 0$. The resulting values are shown in Fig. 4(c). For small and intermediate values of χ, $R^2_{\log}$ remains close to unity, whereas it decreases for the largest size ratios, confirming the progressive departure from a single-exponential description.

To complement this fit-based measure, we define a fit-independent cumulative transport length. The cumulative fraction of the collected mass deposited up to the end of bin n is

$$C_n = \sum_{i=1}^{n} \mu_i, \tag{B2}$$

where μ_i denotes the mass fraction collected in bin i. We define L_{63} as the downslope position at which the cumulative profile, linearly interpolated between bin edges, reaches

$$C(L_{63}) = 1 - e^{-1} \simeq 0.632. \tag{B3}$$

For an ideal continuous exponential profile normalized over $x \geqslant 0$,

$$C(x) = 1 - e^{-x/\ell}, \tag{B4}$$

so that $L_{63} = \ell$.

The experimental estimate of L_{63} is obtained from profiles measured with finite spatial bins of width $\Delta x = 10$ cm.

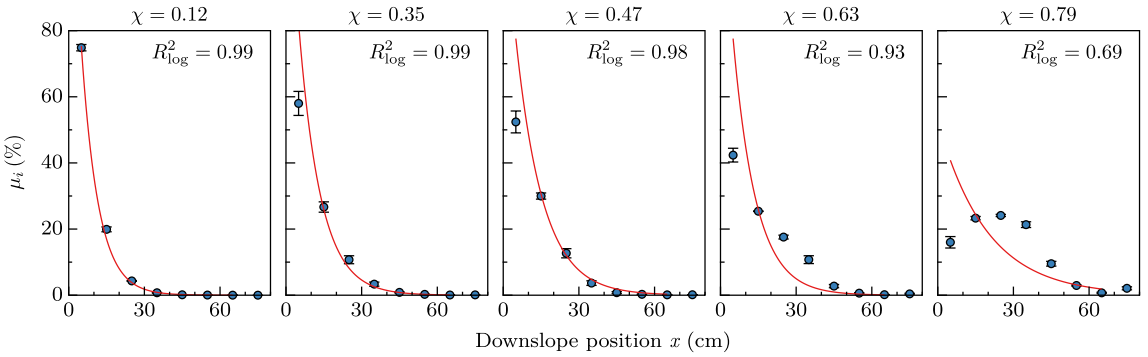


FIG. 7. Experimental deposited-mass profiles for five representative values of $\chi = d/D$ at $M_0 = 1$ kg. Symbols show the mean over three realizations and error bars show one standard deviation. Solid red lines show fits to $\mu^{\mathrm{fit}}(x) = A\exp(-x/\ell)$. The corresponding values of $R^2_{\log}$ are indicated in each panel. The residual collector at $x = 75$ cm is shown but is excluded from the fits and from the calculation of $R^2_{\log}$.

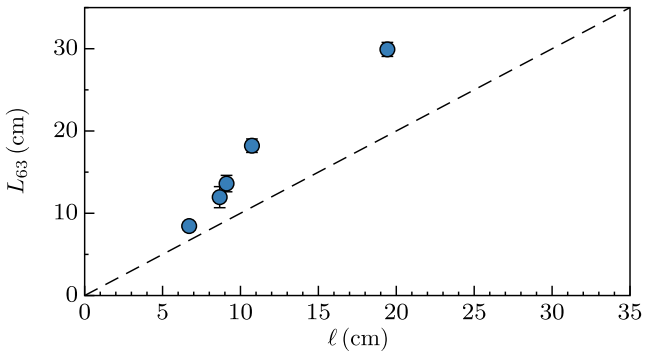


FIG. 8. Cumulative transport length L_{63}, defined by $C(L_{63}) = 1 - e^{-1}$, versus the fitted exponential length ℓ. The dashed line indicates the continuum exponential limit $L_{63} = \ell$.

Consequently, the equality $L_{63} = \ell$ should be regarded as a continuum reference rather than an exact identity for the discretized profiles, particularly at small χ, where ℓ is comparable to or smaller than Δx. Figure 8 shows that L_{63} and ℓ increase together, indicating that ℓ continues to capture the spatial extent of particle transport. Their separation becomes more pronounced at larger χ, consistent with the departure from exponential behavior observed in Fig. 7.

Even when the profile is no longer accurately described by a single exponential, ℓ remains an effective measure of its spatial extent. The finite spatial resolution should nevertheless be considered when interpreting the smallest fitted lengths. The experimental bins have a width of $\Delta x = 10$ cm, while the smallest values satisfy $\ell \lesssim 10$ cm. Resolving this rapid-filtration regime more accurately will therefore require smaller collection bins in future experiments.

[1] W. A. Beverloo, H. A. Leniger, and J. van de Velde, The flow of granular solids through orifices, Chem. Eng. Sci. **15**, 260 (1961).

[2] Y. Forterre and O. Pouliquen, Flows of dense granular media, Annu. Rev. Fluid Mech. **40**, 1 (2008).

[3] C. Mankoc, A. Janda, R. Arévalo, J. M. Pastor, I. Zuriguel, A. Garcimartín, and D. Maza, The flow rate of granular materials through an orifice, Granular Matter **9**, 407 (2007).

[4] A. Janda, I. Zuriguel, and D. Maza, Flow rate of particles through apertures obtained from self-similar density and velocity profiles, Phys. Rev. Lett. **108**, 248001 (2012).

[5] K. To, P.-Y. Lai, and H. K. Pak, Jamming of granular flow in a two-dimensional hopper, Phys. Rev. Lett. **86**, 71 (2001).

[6] A. Marin and M. Souzy, Clogging of noncohesive suspension flows, Annu. Rev. Fluid Mech. **57**, 89 (2025).

[7] I. Zuriguel, A. Garcimartín, D. Maza, L. A. Pugnaloni, and J. M. Pastor, Jamming during the discharge of granular matter from a silo, Phys. Rev. E **71**, 051303 (2005).

[8] I. Zuriguel, D. R. Parisi, R. C. Hidalgo, C. Lozano, A. Janda, P. A. Gago, J. P. Peralta, L. M. Ferrer, L. A. Pugnaloni, E. Clément, D. Maza, I. Pagonabarraga, and A. Garcimartín, Clogging transition of many-particle systems flowing through bottlenecks, Sci. Rep. **4**, 7324 (2014).

[9] N. Standish, The kinetics of batch sieving, Powder Technol. **41**, 57 (1985).

[10] G. K. N. S. Subasinghe, W. Schaap, and E. G. Kelly, Modelling the screening process: A probabilistic approach, Powder Technol. **59**, 37 (1989).

[11] J. Li, C. Webb, S. S. Pandiella, and G. M. Campbell, Discrete particle motion on sieves—A numerical study using the DEM simulation, Powder Technol. **133**, 190 (2003).

[12] K. J. Dong, B. Wang, and A. B. Yu, Modeling of particle flow and sieving behavior on a vibrating screen: From discrete particle simulation to process performance prediction, Ind. Eng. Chem. Res. **52**, 11333 (2013).

[13] R. Maiti, G. Das, and P. K. Das, Granular drainage from a quasi-2D rectangular silo through two orifices symmetrically and asymmetrically placed at the bottom, Phys. Fluids **29**, 103303 (2017).

[14] L. A. Fullard, E. C. P. Breard, C. E. Davies, A. J. R. Godfrey, M. Fukuoka, A. Wade, J. Dufek, and G. Lube, The dynamics of granular flow from a silo with two symmetric openings, Proc. R. Soc. A **475**, 20180462 (2019).

[15] A. Janda, I. Zuriguel, A. Garcimartín, L. A. Pugnaloni, and D. Maza, Jamming and critical outlet size in the discharge of a two-dimensional silo, Europhys. Lett. **84**, 44002 (2008).

[16] P. A. Cundall and O. D. L. Strack, A discrete numerical model for granular assemblies, Géotechnique **29**, 47 (1979).

[17] Y. Guo and J. S. Curtis, Discrete element method simulations for complex granular flows, Annu. Rev. Fluid Mech. **47**, 21 (2015).

[18] A. Cromer, Stable solutions using the Euler approximation, Am. J. Phys. **49**, 455 (1981).